High-energy micrometre-scale pixel direct conversion X-ray detector

Christopher C. Scott,[a] Michael Farrier,[b] Yunzhe Li,[a] Sam Laxer,[a] Parmesh Ravi,[c] Peter Kenesei,[d] Michael J. Wojcik,[d] Antonino Miceli[d] and Karim S. Karim[a,c]*

[a]KA Imaging Inc., 560 Parkside Drive, Unit 3, Waterloo, Ontario, Canada N2L 5Z4, [b]Farrier Microengineering LLC, 616 Petoskey Street, Unit 004, Petoskey, MI 49770, USA, [c]University of Waterloo, 200 University Avenue West, Waterloo, Ontario, Canada N2L 3G1, and [d]X-ray Science Division Advanced Photon Source, Argonne National Laboratory, 9700 South Cass Avenue, Lemont, IL 60439, USA. *Correspondence e-mail: kkarim@uwaterloo.ca

The objective of this work was to fabricate and characterize a new X-ray imaging detector with micrometre-scale pixel dimensions (7.8 µm) and high detection efficiency for hard X-ray energies above 20 keV. A key technology component consists of a monolithic hybrid detector built by direct deposition of an amorphous selenium film on a custom designed CMOS readout integrated circuit. Characterization was carried out at the synchrotron beamline 1-BM-B at the Advanced Photon Source of Argonne National Laboratory. The direct conversion detector demonstrated micrometre-scale spatial resolution with a 63 keV modulation transfer function of 10% at Nyquist frequency. In addition, spatial resolving power down to 8 µm was determined by imaging a transmission bar target at 21 keV. X-ray signal linearity, responsivity and lag were also characterized in the same energy range. Finally, phase contrast edge enhancement was observed in a phase object placed in the beam path. This amorphous selenium/CMOS detector technology can address gaps in commercially available X-ray detectors which limit their usefulness for existing synchrotron applications at energies greater than 50 keV; for example, phase contrast tomography and high-resolution imaging of nanoscale lattice distortions in bulk crystalline materials using Bragg coherent diffraction imaging. The technology will also facilitate the creation of novel synchrotron imaging applications for X-ray energies at or above 20 keV.

1. Introduction

Currently available X-ray imaging detectors can be limited in combining high spatial resolution and high detection efficiency for X-ray energies above 20 keV. Hybrid X-ray detectors reported to date generally have adequate detection efficiency for hard X-rays using high-Z sensor materials but have relatively large ($\geq$50 µm) pixel dimensions (Buton *et al.*, 2014; Pennicard *et al.*, 2014; Bellazzini *et al.*, 2015; Philipp *et al.*, 2020; Greiffenberg *et al.*, 2021). These direct conversion detectors feature high sensitivity, high count rates and energy discrimination (with photon-counting pixels) but remain limited in pixel size due to the need to bump-bond individual pixels to the photoconductor sensor (*e.g.* GaAs, CdTe, CdZnTe). Scintillator-based indirect conversion X-ray detectors (Martin & Koch, 2006), on the other hand, can resolve fine features using small-pixel CMOS active pixel sensors (APS) and magnifying optics but are non-optimal for energies greater than 20 keV. This is due to the requirement that the scintillator needs to be thin enough to fall within the depth of field of the objective lens for optimal spatial resolution. Additionally, there is a trade-off between absorption efficiency and spatial resolution of the scintillator. Thicker scintillators can provide equal or
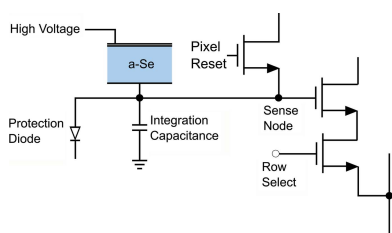
better absorption efficiency compared with photoconductors but result in increased internal optical scatter and consequently a degradation of spatial resolution. Novel high-density, high-efficiency scintillators may reduce or eliminate this performance gap (Marton *et al.*, 2015, 2020). However, indirect conversion detectors still rely on optics that can cause spatial distortion and limit the field of view and are often bulky, resulting in form factors that can be challenging to position. To date, the performance limitations of direct and indirect commercial off-the-shelf X-ray detectors have restricted the scope of experiments that can be conducted at synchrotron light sources at high energies, thus impeding progress in understanding complex nanoscale structures in materials through diffraction and tomographic imaging techniques. In particular, Bragg coherent diffraction imaging (BCDI) can provide insight into the structure and dynamics of crystalline materials when implemented at highly penetrating X-ray energies (*i.e.* >50 keV) amenable to accessing *in situ* environments and deeply buried volumes (Maddali *et al.*, 2019). However, the compression of reciprocal space at high energies creates challenges for existing detectors to provide sufficient spatial sampling (Maddali *et al.*, 2018). BCDI would greatly benefit from efficient, direct conversion detectors with micrometre-scale resolution.

Amorphous selenium (a-Se) is a mature large-area thermally evaporated photoconductor that has been used extensively in flat-panel X-ray imagers (Kasap *et al.*, 2011). The imaging performance at visible and X-ray wavelengths for a small 8 pixel × 8 pixel array, composed of a thin film of a-Se photoconductor directly deposited on a CMOS passive pixel sensor (PPS) readout device, was reported by Majid *et al.* (2011). Initial X-ray imaging results for hybridized a-Se on a CMOS readout integrated circuit (ROIC) were reported in 2014 and featured 25 µm pixel pitch and a 640 × 640 CMOS APS readout array with a 12-bit column analogue-to-digital converter (Scott *et al.*, 2014). The high detection efficiency at high X-ray energies, combined with low-noise CMOS pixel performance was confirmed using standard medical X-ray sources (Mo and W targets).

Addressing demands for high-energy and high spatial resolution X-ray imaging for materials research, a 1 megapixel detector (1000 pixels × 1000 pixels), comprised of an a-Se/CMOS APS readout hybrid imaging array of 7.8 µm pixel pitch (plus camera components), was designed and fabricated. The a-Se/CMOS hybrid detector technology enables both high quantum efficiency for hard X-ray energies up to 100 keV as well as close spacing of pixels with minimal charge spreading. The patented detector technology (Karim & Abbaszadeh, 2016; Karim *et al.*, 2020) was originally developed at the University of Waterloo (Parsafar *et al.*, 2015; Scott *et al.*, 2015; Scott, 2019). With a microfocus X-ray source, detector prototypes have demonstrated micrometre-scale spatial resolution, plus a significant increase in detection efficiency at 60 kV compared with commercially available CMOS indirect conversion X-ray detectors.

In this work, characterization of the detector was carried out using the 1-BM-B beamline at the Advanced Photon Source of Argonne National Laboratory (APS/ANL). Fundamental parameters such as X-ray signal linearity and responsivity, modulation transfer function (MTF), resolving power, and image lag were quantified, and phase contrast imaging was conducted.

2. Materials and methods

2.1. Detector technology

The custom three transistor (3T) pixel design is illustrated in Fig. 1. A charge sense node connected to a metal pad receives signal charge directly from the layer of photoconductive a-Se, which has been directly deposited on the CMOS ROIC. The pixel input capacitance is 58 fF, with an operating range of 2.3 V. The signal is sampled by a 14-bit analogue-to-digital converter with a 250 µV per digital number (DN) precision. This results in a theoretical pixel conversion gain of 90.6 electrons per DN, and a full well capacity of 833 000 electrons. With a pixel input capacitance of 58 fF the kTC noise is 96 electrons. With protection diode leakage and reset device leakage current (12.8 fA) there is a shot noise of 151 electrons. This results in approximately 180 electrons of readout noise. The CMOS leakage current is, in part, due to the mixed signal process technology node employed and the long integration time periods. In addition, the 3T pixel design does not allow for correlated double sampling (CDS).

The a-Se layer thickness was 100 µm and becomes photosensitive when a high bias voltage is applied to a top electrode that generates an internal electric field typically in the range 5–10 V µm^{-1}. No blocking layers were employed in this work. Depending on the bias polarity, a-Se may be operated in either hole- or electron-collection mode, with differing performance based on charge carrier mobilities, lifetimes, as well as variations in other parameters such as frame rate and dark/leakage current. The 3T pixel design can operate in either collection mode by adjusting the reset voltage; however, the superior carrier mobility-lifetime product of holes compared with electrons can improve the stability of X-ray responsivity in hole-collection mode (Zhao & Zhao, 2005). For this reason, the pixel protection diode was designed to trigger for hole-
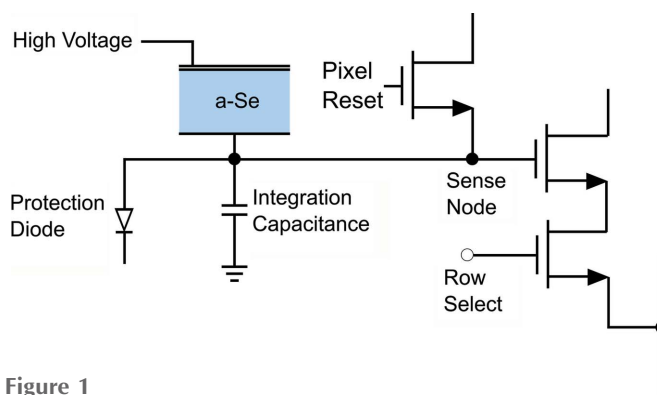

Figure 1
Custom three transistor (3T) pixel design of the CMOS ROIC.

collection mode and the detector was operated in this mode here. The resulting dark/leakage current in hole-collection mode was 0.7 pA mm^{-2} at 5 V μm^{-1}.

2.2. Synchrotron beamline

Characterization of the detector was performed using the direct, monochromatic X-ray beam available from the 1-BM-B beamline at APS/ANL. Supporting apparatus included resolution targets, a polished tungsten edge, attenuators, filters, X-ray slits, phase objects, pinholes and flux sensors available through the detector pool. Characterization was performed at 21 keV and 63 keV X-ray energies. The 21 keV beam was obtained from the Si (111) reflection of the monochromator. Higher orders of reflection were minimized by detuning the second crystal in the monochromator and a 7 mm glass filter was used to reduce the intensity of the X-rays. A 63 keV X-ray energy was obtained from the Si (333) reflection and Mo foils were used to attenuate the Si (111) reflection (21 keV transmission < 0.01%) such that the 63 keV component dominates. Both 7 mm × 4 mm and 7 mm × 2 mm slit apertures were used.

2.3. Linearity

The detector response linearity with respect to X-ray exposure was measured at 21 keV and 63 keV by varying the integration time. For both energies, frames were acquired at 250 ms, 500 ms, 750 ms and 1000 ms integration times. In all cases the biasing electric field was held constant at 5 V μm^{-1}. After dark and X-ray response non-uniformity correction, the mean signal was acquired from a region of interest (ROI) of 500 pixels (columns) by 100 pixels (rows) using a 10-frame average. At each energy, the ROI was chosen to be a region of exposure uniformity. The pixel signal was converted from the arbitrary unit of DN to electrons using the pixel conversion gain of 90.6 electrons per DN and was then computed as a percentage of the full well capacity (FWC) of 883 000 electrons.

2.4. Responsivity

Detector responsivity, defined as charge collected on the pixel per absorbed X-ray photon, was measured with varying applied electric field between 4 V μm^{-1} and 5.8 V μm^{-1} at 21 keV and 63 keV X-ray photon energies. The experimental responsivity, R_{meas}, was calculated using

$$R_{meas} = \frac{g S_{meas}}{\eta(E, L)\, \phi_{meas}\, t_{int}}. \tag{1}$$

The pixel signal, S_{meas}, in units of DN was acquired from an ROI size of 500 pixels (columns) by 100 pixels (rows) using a 5 to 10 frame average after dark and X-ray response non-uniformity correction. The ROIs differ from those in Section 2.3 due to beam positioning. The pixel conversion gain, g, is 90.6 electrons per DN. The quantum attenuation efficiency, η, of the a-Se photoconductor has a dependence on X-ray photon energy, E, and photoconductor thickness, L. At 21 keV and 63 keV the values of η are 84% and 9%, respec-

Table 1
K-fluorescence related parameters for a-Se (Kabir & Kasap, 2002; Dance & Day, 1985).

Photoelectric fraction of total attenuation, f_{pe}	0.98 (21 keV), 0.88 (63 keV)
K-shell contribution to photoelectric interaction, P_K	0.88
K-fluorescence yield, Y_K	0.593
Weighted average K-fluorescence energy, $\bar{E}_K$	11.375 keV
Average re-absorption probability, P_R	0.67 (21 keV), 0.68 (63 keV)

tively, for an a-Se density of 4.4 g cm^{-3} and thickness of 100 μm. The photon flux (photons s^{-1}) was measured by a silicon PIN photodiode with an independent calibration (Krumrey et al., 2004). The average flux density (photons s^{-1} mm^{-2}) was then calculated using the slit/beam size. From this, the flux per pixel (photons s^{-1} pixel^{-1}), ϕ_{meas}, was calculated using the full pixel area. For completeness, the flux per pixel will be reported for all characterizations where it was measured. The geometric fill factor of the pixel is approximately 26%; however, we assume 100% effective fill factor due electric field line shaping near the pixels (Pang et al., 1998; Hunt et al., 2004). All 21 keV frames were acquired with an integration time, t_{int}, of 1 s and all 63 keV frames were acquired at 250 ms.

To model the theoretical responsivity the conversion gain describing the energy cost per photogenerated electron–hole pair (EHP) is required. The conversion gain of a-Se, $W_{\pm}$, does not obey Klein's relationship, applicable to many crystalline and non-crystalline semiconductors, where conversion gain is proportional to the bandgap energy. In the case of a-Se it also depends on X-ray photon energy, E, and electric field, F. An empirical expression derived from a columnar recombination model fitted to experimental measurements of a-Se conversion gain is used as an alternative (Kabir et al., 2019). For 21 keV and 63 keV the values of $W_{\pm}$ at 5.5 V μm^{-1} are 101 eV per EHP and 70 eV per EHP, respectively. In this energy range, the amount of incident photon energy absorbed in a-Se, E_{abs}, is a combination of the primary photon absorption and K-fluorescence re-absorption (Kabir & Kasap, 2002). The theoretical responsivity, R_{th}, is then given by

$$R_{th} = \frac{E_{abs}}{W_{\pm}(E, F)} = \frac{1}{W_{\pm}(E, F)} \left(\frac{\mu_{en}}{\mu} E + f_{pe}(E)\, P_K Y_K \bar{E}_K P_r \right). \tag{2}$$

Charge collection efficiency was assumed to be high (~100%) since the low-end of the hole mobility-lifetime product is on the order of 10^{-6} cm^2 V^{-1} (Kasap et al., 2011), giving a hole range four times the a-Se thickness at 4 V μm^{-1}, the low-end of our applied electric field. The quantum attenuation efficiency and ratios of the energy absorption coefficient to the linear attenuation coefficient, μ_{en}/μ, and the photoelectric fraction of total attenuation, f_{pe}, were calculated from a NIST database (Hubbell & Seltzer, 2004). K-fluorescence related parameters are described in Table 1. The empirical expression for $W_{\pm}$ was based on fitting experimental a-Se conversion gain measurements over a large energy range from 16.5 keV to

research papers

1.25 MeV by methods such as pulse height spectroscopy and xeroradiographic discharge. Furthermore, the expression used in fitting was derived from a columnar recombination model by numerically solving the continuity equation considering carrier drift, diffusion and bimolecular recombination.

2.5. Modulation transfer function

The MTF was measured using the slanted-edge technique (Samei *et al.*, 1998). Edge images were acquired at 21 keV and 63 keV. A polished tungsten straight edge was positioned at an angle relative to the detector rows such that the position of the edge was phase-shifted in each column. The edge profiles of each column were combined to generate an oversampled edge-spread function (ESF) with sub-pixel sampling at one-tenth the pixel pitch. The derivative of the sub-pixel sampled ESF after binning was used to determine the line spread function (LSF), which was then Fourier transformed and scaled by the pixel pitch to determine the pre-sampling MTF.

The MTF was modelled using the known spread of absorbed energy by the inherent X-ray processes in a-Se, which are weighted by their relative energy deposition (Que & Rowlands, 1995). It is known that in the 21–63 keV energy range the photoelectric effect is the dominant source of energy deposition. At energies above the K-edge (12.7 keV) it can be assumed that the primary photoelectron is ejected from the K-shell because of a significantly larger interaction cross section. The primary photoelectron energy deposition was modelled as a spherically symmetric spatial profile with a Gaussian envelope determined by the continuous-slowing-down approximation (CSDA). The re-absorption or escape of K-fluorescent photons at lateral distances from the primary interaction location, which is significant at a-Se thicknesses for hard X-rays, is also considered. At low energies, long-range K-fluorescence re-absorption results in a significant low-frequency drop in MTF while the roll-off at high spatial frequencies caused by the primary photoelectron is insignificant owing to low kinetic energy. At high energies K-fluorescence generation is significantly reduced, and the effect of the primary photoelectron at high spatial frequencies is dominant due to high kinetic energy.

2.6. Spatial resolving power

A JIMA RT RC-05 transmission bar target was used to measure resolving power. The absorption of the patterned gold bars of 1 μm thickness is sufficient at 21 keV to create high-contrast bar pattern images. This was not the case at the higher energy of 63 keV due to negligible attenuation (<0.2%).

2.7. Lag

Image lag is the residual signal contribution in a frame caused by charge carriers photogenerated or injected during previous frames. The phenomenon exists due to charge trapping (and subsequent de-trapping) in the a-Se layer, and enhanced charge injection during photogeneration (Zhao & Zhao, 2005). Lag in a-Se is dependent on several factors including electric field strength, layer thickness, other layers (*e.g.* blocking layers) and X-ray exposure. At 100 μm thick the detector has an a-Se layer over an order magnitude larger than the pixel size (7.8 μm). This geometry results in the small pixel effect (SPE) (Barrett *et al.*, 1995), where pixels only sense charge carriers travelling towards them once they are nearly collected at the pixel electrode. This type of unipolar charge sensing means that the pixel is relatively insensitive to the de-trapping of electrons in hole-collection mode, reducing de-trapping lag. However, the lack of blocking layers means injection current lag is not supressed.

Pin hole apertures of 50 μm and 200 μm diameter in a tungsten substrate were imaged while the detector was scanned in the horizontal direction at a speed of 25.6 pixels^{-1} (or 0.2 mm s^{-1}) in a 63 keV beam. Frames were captured at a rate of 2 fps, enabling measurement of the lag response (being the residual signal read out in successive frames). The lag signal was measured at three selected ROIs along the path of the pinhole and the resulting profiles were plotted as a function of time after initial exposure. The first ROI was chosen to be the initial position of the pinhole before scanning. The second ROI was chosen to be at a small offset to the first ROI. Finally, the third ROI was chosen to be at a large offset from the initial ROI, closer to the end of the pinhole scan. These regions were chosen to analyze the consistency of the resulting lag. At each position, a circular ROI smaller than the pinhole size (80% of the radius) to ignore edge effects was used to determine the mean signal within the region.

2.8. Phase contrast

Phase contrast arises as variation in refractive index and the thickness of matter comprising the medium alters the shape of the X-ray wavefront. With free-space propagation the altered X-ray wavefront is converted to intensity changes at the detector. This can be particularly useful when an object presents poor conventional absorption contrast (*e.g.* soft biological tissue or other low-density materials such as polymers). Instead, the closely spaced pixel pitch and minimal charge spreading can be used to capture enhancement of edge features at material boundaries where the refractive index changes abruptly.

Evidence of phase contrast edge enhancement at 21 keV was found in images of a phase object comprising air bubble features in epoxy resin (bisphenol A diglycidyl ether). The bubbles were approximately 91 cm from the detector. To investigate further, free-space propagation of an analytical map of the spherical cavity was modelled using Fresnel diffraction. The resulting image was multiplied in the frequency domain with the theoretical MTF to simulate blurring. Finally, the image was interpolated to the detector pixel pitch. A cross section of this modelled bubble was then found on a slice passing through its centre, and a similar profile was found for the experimental bubble. Both these profiles were then normalized and overlaid to create a final edge-enhancement comparison image.

3. Results

3.1. Linearity

With varying integration time, the linearity of the detector response to X-ray exposure was plotted in Fig. 2(a) as a percentage of the full well capacity of 883 000 electrons. The measured flux per pixel was 2204 photons s^{-1} pixel^{-1} at 21 keV and 6865 photons s^{-1} pixel^{-1} at 63 keV. Both 21 keV and 63 keV energies showed a high degree of linearity up to 26% and 34% of the full well capacity (having R^2 values of 0.99774 and 0.99790), respectively.

3.2. Responsivity

The measured responsivity values were plotted with the empirical model in Fig. 2(b). The measured flux per pixel was 2381 photons s^{-1} pixel^{-1} and 3851 photons s^{-1} pixel^{-1} for 21 keV and 63 keV, respectively. At 21 keV there is relatively close agreement between the measured and modelled values
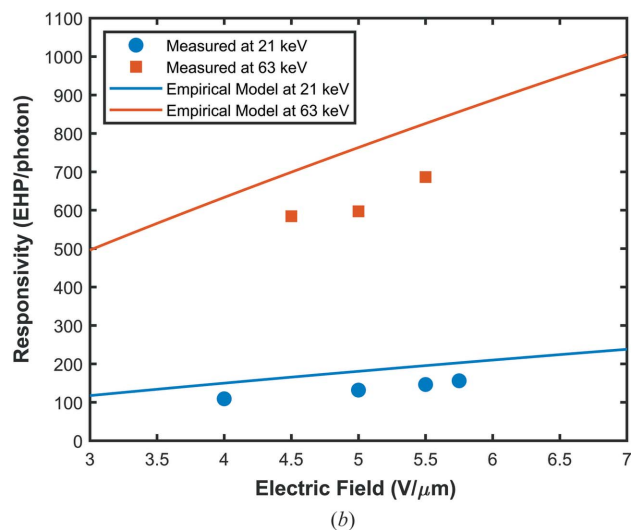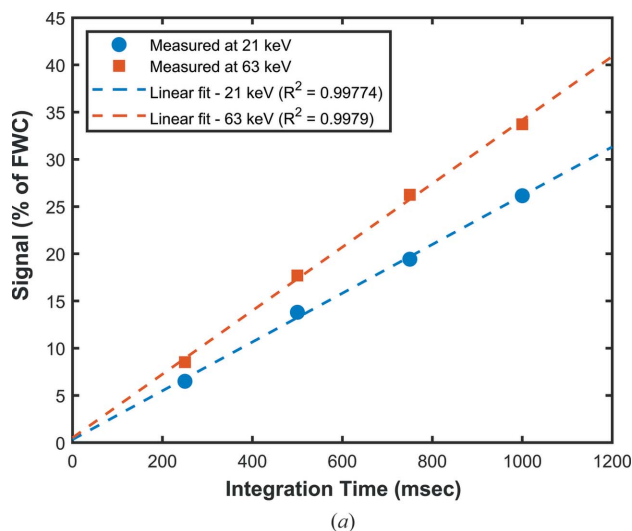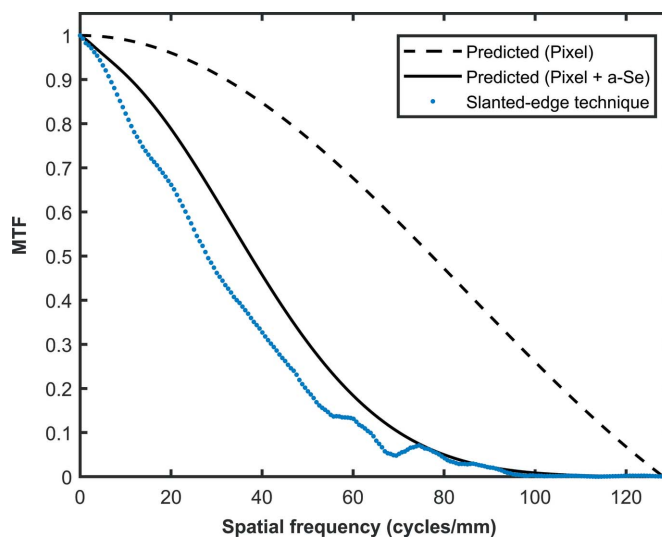
Figure 3
MTF measured at 63 keV using the slanted-edge technique. The model prediction is shown for the pixel itself, as well as the combined contribution from the pixel and a-Se.

(<9% deviation). At the higher energy (63 keV) the measured and modelled response have a larger discrepancy (<17%).

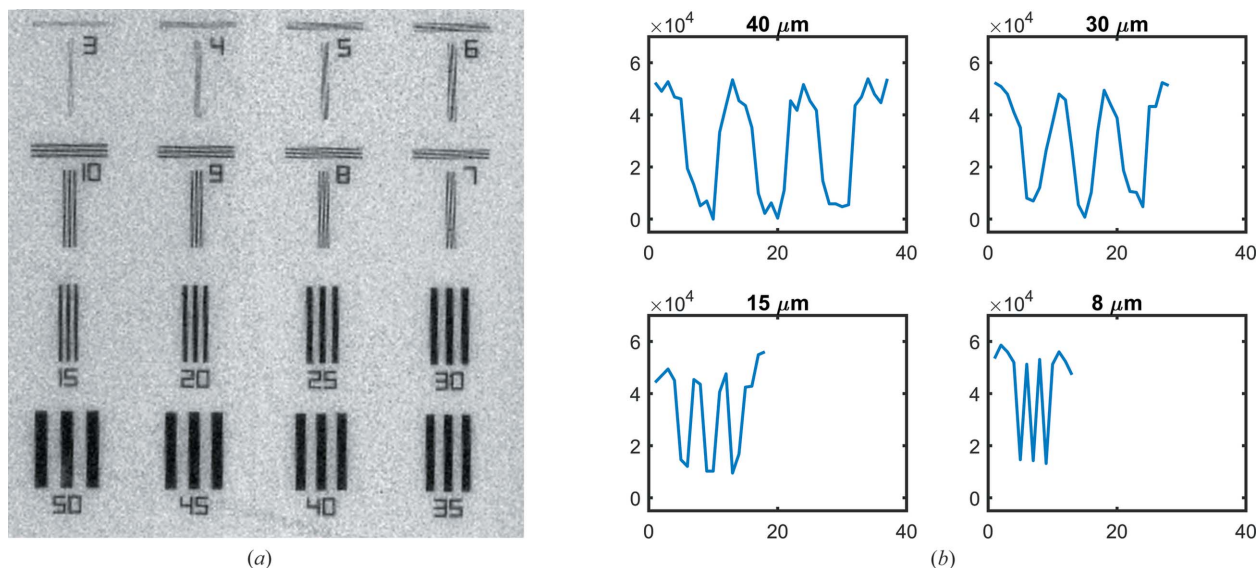### 3.3. Modulation transfer function

The MTF measured using the slanted-edge technique and the model predictions are shown in Fig. 3. A spatial nonuniformity in the beam intensity affected the edge image results. In the case of the 21 keV energy, the edge information was not preserved and thus the MTF was not obtainable. The measured flux per pixel at 63 keV was 6865 photons s^{-1} pixel^{-1}. At this energy, the dominant effect of the primary photoelectron range is clear with a roll-off at high spatial frequencies which is more rapid than in the pixel response. The measured MTF is generally lower than the prediction. However, the 10% MTF at the Nyquist frequency of 64 cycles mm^{-1} is within a few percent of the modelled data.

3.4. Spatial resolving power

Spatial resolution bar imaging was conducted at 21 keV. Fig. 4 illustrates the resolving power of the detector using the JIMA RT RC-05 transmission bar target. The absorption of gold patterns at 1 µm thickness is sufficient at 21 keV to create high-contrast bar pattern images with a contrast-to-noise ratio of approximately 10 for bars spaced at 8 µm (pixel pitch is 7.8 µm).

3.5. Image lag

The images of the pinhole scans, and the resulting lag signal time profiles in the three selected ROIs are shown in Fig. 5. The measured flux per pixel was 6865 photons s^{-1} pixel^{-1}. In the case of the 50 µm pinhole, the measured lag signal in the initial ROI [Fig. 5(c), red] was 5.6% at 1 s and 0% at 10 s. The lag signal measured offset on the path from the initial pinhole position [Fig. 5(c), green] was 2.3% at 1 s and 0.9% at 10 s.

(a)

(b)

Figure 2
(a) X-ray signal relative to the FWC as a function of integration time. Linear fits are shown as dashed lines for both energies. (b) X-ray responsivity as a function of the electric field in 100 µm-thick a-Se. The empirical model is shown along with the measured data.

Figure 4
(a) JIMA RT RC-05 bar pattern image acquired at 21 keV. (b) Contrast cross sections for three bars spaced at 40 µm, 30 µm, 15 µm and 8 µm. The signal level in DN is plotted versus pixels.
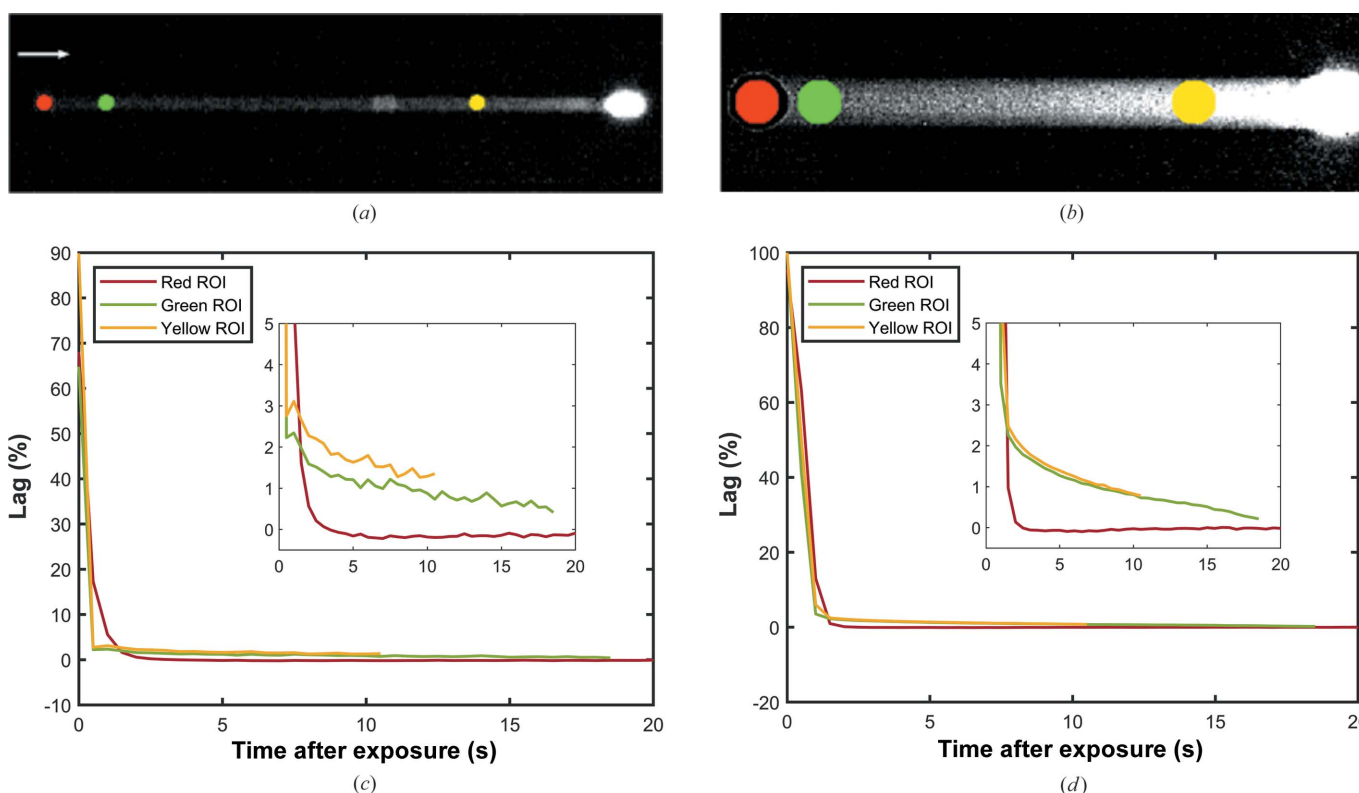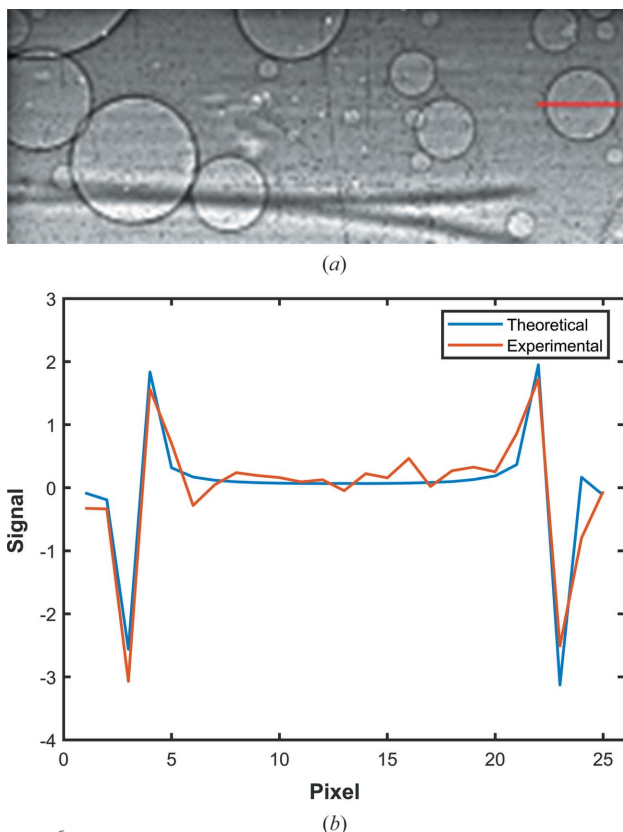

Figure 5
Images of the pinhole scan (direction of motion indicated by the white arrow) and residual lag signal plots versus time after initial exposure at three ROIs (red, green and yellow) for (a, c) a 50 µm pinhole and (b, d) a 200 µm pinhole. Inlaid in the residual lag plot is a magnified view of the data from 0% to 5% lag over the full scan duration.

Similarly, for the larger offset [Fig. 5(c), yellow], the lag signal was 3.1% at 1 s and 1.3% at 10 s. The 200 µm pinhole [Fig. 5(d)] resulted in similar lag characteristics. The initial ROI had a lag signal of 1% at 1 s and 0% at 10 s. The ROI slightly offset from the initial position experienced 2.3% lag at 1 s and 0.7% at 10 s, and the larger offset ROI experienced 2.5% lag at 1 s and 0.8% at 10 s.

3.6. Phase contrast

Evidence of phase contrast edge enhancement is seen in Fig. 6(a) which depicts an image of air bubble features formed in epoxy resin. The radius of the air bubble was estimated to be approximately 80 µm, found by counting the number of pixels present in the image of the air bubble and scaling by the

(a)

(b)

Figure 6
(a) Image of air bubbles in epoxy resin. The red horizontal line in the image represents the cross-section used to generate the edge enhanced profile. (b) Comparison of the theoretical and experimental edge enhancement profile.

pixel pitch. This result is supported by agreement between the edge enhanced bubble cross-section and the model for propagation-based phase contrast in Fig. 6(b) using the best estimates of the experimental conditions.

4. Discussion

A 1-megapixel a-Se/CMOS direct conversion detector with 7.8 μm pixel pitch was designed, fabricated and characterized. The expected theoretical performance matches well with the experimental findings. The detector photon response was shown to be linear with integration time at 21 keV and 63 keV X-ray energies up to 26% and 34% of the full well capacity, respectively. The X-ray responsivity was reported in good agreement with the expected change in a-Se conversion gain as a function of X-ray energy and applied electric field. The deviation between measured and modelled responsivity at 21 keV was <9% and at 63 keV the deviation was greater at <17%. The greater discrepancy at 63 keV is not fully understood and requires further investigation. The readout noise of the developed detector is around 180 electrons RMS which, when coupled with an a-Se conversion gain of 70 eV/EHP at 63 keV and 5.5 V μm^{-1}, can achieve a signal-to-noise ratio of 5 which enables single-photon detection at high energy.

Spatial resolution was characterized at 63 keV using the slanted-edge technique. A spatial non-uniformity in the photon flux from the source created non-ideal conditions for MTF calculations, which may have resulted in abnormalities in the measured MTF data plot. However, the 10% MTF at Nyquist frequency is within a few percent of the modelled data and represents a significant improvement in spatial resolution for direct conversion X-ray detectors. At low energy (21 keV) sufficient absorption contrast was generated using a transmission bar target to demonstrate resolving power down to 8 μm.

Lag behaviour was studied by scanning two circular pinholes. Because both lag scans were performed at the same rate, the larger pinhole resulted in each pixel along the path being exposed for a longer duration, particularly the pixels close to the central axis of the scan as they are exposed for the full diameter of the pinhole. Despite the synchronization challenges of the pinhole motion, relatively low frame rate and the rolling shutter, both pinhole sizes resulted in similar lag profiles for the ROIs offset from the initial exposure. This suggests that, within this experimental error, the lag is proportional to X-ray exposure. On the other hand, the most rapid overall drop in lag signal was in the initial ROI for both pinholes. This region had been exposed for approximately 5 s before the scan commenced and it is possible that the added exposure decreased the a-Se responsivity in that region versus the pixels along the path after the scan began. This is typically attributed to charge recombination due to trapped charge in a-Se from previous X-ray exposures (Zhao & Zhao, 2005). In this case it is possible that the enhanced injection charge recombined with trapped electrons. In general, unremarkable lag performance was expected due to the lack of blocking layers and the relatively low operating electric field.

The strong agreement between experimental and theoretical results indicates a fundamental understanding of the inherent X-ray interaction processes in a-Se. An empirical model was used to calculate the a-Se conversion gain as a function of X-ray energy and applied electric field. The theoretical MTF was modelled using the known spread of absorbed energy in a-Se due to the dominant photoelectric interaction with the K-shell as well as the corresponding reabsorbed fluorescent X-rays. Finally, the material boundary edge enhancement in the phase object was consistent with the Fresnel diffraction of the spatially coherent X-ray beam resolved by the detector.

Based on these results we believe the detector presented has a unique combination of high spatial resolution and high detection efficiency for hard X-rays compared with other direct conversion detectors reported in the literature or in commercial use, e.g. c-Si, CdTe or GaAs-based detectors. This detector fills a niche for high spatial resolution X-ray detectors capable of detecting energies above 20 keV and where readout speed is not critical. A good case would be BCDI where high energy can be used to investigate thick samples (Maddali et al., 2018, 2019, 2020). The detector field of view (FOV) is 7.8 mm, so a sample diameter up to this size can be used for a single FOV tomography scan. At the APS/ANL bending magnet beamline the beam can be approximately 1 cm in size, and the

intensity at higher energies is low, so the slow speed of the detector is not a problem.

Future work includes developing improved detector performance for image lag, responsivity drift, frame rate, conversion gain, as well as stabilizing the a-Se film from substrate strain and thermal effects which can cause crystallization. Hole and electron blocking layers (Abbaszadeh *et al.*, 2012; Frey *et al.*, 2019) must be added to suppress dark/injection current, permitting higher operating fields and consequently better conversion gain. Crystallization of the a-Se film from substrate shear-strain or thermal effects can be suppressed by introducing a soft polymer buffer layer (Lindberg *et al.*, 2014) such as polyimide (Karim & Abbaszadeh, 2016). Although the current and next design iterations of the detector have relatively low frame rates ($\leq$5 fps), a-Se photoconductors are not limited to static imaging. Unipolar charge sensing can be leveraged to increase a-Se speed by only sensing the high mobility-lifetime product holes, either through the SPE or novel pixel structures (Goldan *et al.*, 2012). Such pixel structures have shown improved lag performance (Goldan *et al.*, 2010), *e.g.* 1% lag has been demonstrated at 30 fps (Camlica *et al.*, 2018). Planned lag and responsivity drift improvement strategies include the use of SPE and different blocking layers to enable higher electric fields. We also plan to investigate smaller pixel sizes and larger FOVs. Finally, verifying the long-term radiation hardness and lifetime of the detector is crucial. Hybrid a-Se detectors have been used in clinical mammography applications for the past two decades; however, a-Se can exhibit temporary and permanent damage due to radiation effects for some applications (Kasap *et al.*, 2011). Challenges related to radiation effects in CMOS must also be studied (Dodd *et al.*, 2010).

A performance summary of the detector is shown in Table 2 and is compared with the next design iteration.

5. Conclusions

A high-energy micrometre-scale pixel direct conversion detector was fabricated and evaluated using the 1-BM-B beamline at the APS/ANL. The performance of the detector was investigated through the measurement and analysis of a series of metrics. The measurements largely confirm modelled predictions for linearity, responsivity, MTF, resolving power, lag and phase contrast. In particular, the MTF at high spatial frequencies measured using hard X-rays demonstrates the successful development of a detector technology that can advance research in materials science applications such as phase contrast tomography and high spatial resolution imaging of nanoscale lattice distortions in bulk crystalline materials using BCDI at energies greater than 50 keV. The technology will also facilitate the creation of novel beamline imaging applications at X-ray energies at or above 20 keV.

Acknowledgements

The authors acknowledge the University of Waterloo for access to the Giga-to-Nanoelectronics (G2N) center.

Table 2
Summary of the a-Se/CMOS direct conversion X-ray detector performance specifications compared with the next design iteration.

	1-Megapixel detector (current design iteration)	16-Megapixel detector (next design iteration)
Pixel size (μm)	7.8	8
Array size (pixels)	1000×1000	4096×4096
Field of view (mm)	7.8×7.8	32.8×32.8
Frame rate (fps)	5	2
Full well capacity (electrons)	883×10^3	858×10^3
RMS noise (electrons)	180 at 5 fps	150 (theoretical)
Detector applied electric field (V μm^{-1})	4–5.8	$\geq$10
Quantum efficiency (%)	84 at 21 keV, 9 at 63 keV	
a-Se conversion gain	101 eV per EHP at 21 keV and 5.5 V μm^{-1} 70 eV per EHP at 63 keV and 5.5 V μm^{-1}	TBD†
Pixel conversion gain (electrons)	90.6 per DN (theoretical)	58 per DN (theoretical)
Responsivity	156 EHP per photon at 21 keV and 5.8 V μm^{-1} 687 EHP per photon at 63 keV and 5.5 V μm^{-1}	TBD†
MTF	50% at 1/2 Nyquist (32 cycles mm^{-1}), 63 keV and 5 V μm^{-1}	TBD†
Image lag	1–3% at 1 s	TBD†

† Similar or improved performance expected.

References

Abbaszadeh, S., Allec, N., Ghanbarzadeh, S., Shafique, U. & Karim, S. K. (2012). *IEEE Trans. Electron Devices*, **59**, 2403–2409.
Barrett, H. H., Eskin, J. D. & Barber, H. B. (1995). *Phys. Rev. Lett.* **75**, 156–159.
Bellazzini, R., Brez, A., Spandre, G., Minuti, M., Pinchera, M., Delogu, P., de Ruvo, P. L. & Vincenzi, A. (2015). *J. Instrum.* **10**, C01032.
Buton, C., Dawiec, A., Graber-Bolis, J., Arnaud, K., Bérar, J. F., Blanc, N., Boudet, N., Clémens, J. C., Debarbieux, F., Delpierre, P., Dinkespiler, B., Gastaldi, T., Hustache, S., Morel, C., Pangaud, P., Perez-Ponce, H. & Vigeolas, E. (2014). *Nucl. Instrum. Methods Phys. Res. A*, **758**, 44–56.
Camlica, A., Lee, D. L. & Karim, K. S. (2018). *Proc. SPIE*, **10573**, 105735W.
Dance, D. R. & Day, G. J. (1985). *Phys. Med. Biol.* **30**, 259–262.
Dodd, P. E., Shaneyfelt, M. R., Schwank, J. R. & Felix, J. A. (2010). *IEEE Trans. Nucl. Sci.* **57**, 1747–1763.
Frey, J. B., Sadasivam, K., Belev, G., Mani, H., Laperriere, L. & Kasap, S. (2019). *J. Vac. Sci. Technol. A*, **37**, 061501.
Goldan, A. H., Tousignant, O., Karim, K. S. & Rowlands, J. A. (2012). *Appl. Phys. Lett.* **101**, 213503.
Goldan, A. H., Tousignant, O., Laperrière, L. & Karim, K. S. (2010). *Appl. Phys. Lett.* **96**, 053507.

Greiffenberg, D., Andrä, M., Barten, R., Bergamaschi, A., Brückner, M., Busca, P., Chiriotti, S., Chsherbakov, I., Dinapoli, R., Fajardo, P., Fröjdh, E., Hasanaj, S., Kozlowski, P., Cuenca, C. L., Lozinskaya, A., Meyer, M., Mezza, D., Mozzanica, A., Redford, S., Ruat, M., Ruder, C., Schmitt, B., Thattil, D., Tinti, G., Tolbanov, O., Tyazhev, A., Vetter, S., Zarubin, A. & Zhang, J. (2021). *Sensors*, **21**, 1550.

Hubbell, J. H. & Seltzer, S. M. (2004). *Tables of X-ray Mass Attenuation Coefficients and Mass Energy-Absorption Coefficients* (version 1.4). National Institute of Standards and Technology, Gaithersburg, MD, USA. https://www.nist.gov/pml/x-ray-mass-attenuation-coefficients.

Hunt, D. C., Tousignant, O. & Rowlands, J. A. (2004). *Med. Phys.* **31**, 1166–1175.

Kabir, M. Z., Arnab, S. M. & Hijazi, N. (2019). *J. Mater. Sci. Mater. Electron.* **30**, 21059–21063.

Kabir, M. Z. & Kasap, S. O. (2002). *J. Phys. D Appl. Phys.* **35**, 2735–2743.

Karim, K. S. & Abbaszadeh, S. (2016). US Patent No. 9 269 838. Washington, DC: US Patent and Trademark Office.

Karim, K. S., Scott, C. & Li, Y. (2020). US Patent No. 10 627 530. Washington, DC: US Patent and Trademark Office.

Kasap, S., Frey, J. B., Belev, G., Tousignant, O., Mani, H., Greenspan, J., Laperriere, L., Bubon, O., Reznik, A., DeCrescenzo, G., Karim, K. S. & Rowlands, J. A. (2011). *Sensors*, **11**, 5112–5157.

Krumrey, M., Büermann, L., Hoffmann, M., Müller, P., Scholze, F. & Ulm, G. (2004). *AIP Conf. Proc.* **705**, 861–864.

Lindberg, G. P., O'Loughlin, T., Gross, N., Reznik, A., Abbaszadeh, S., Karim, K. S., Belev, G., Hunter, D. M. & Weinstein, B. A. (2014). *Can. J. Phys.* **92**, 728–731.

Maddali, S., Allain, M., Cha, W., Harder, R., Park, J.-S., Kenesei, P., Almer, J., Nashed, Y. & Hruszkewycz, S. O. (2019). *Phys. Rev. A*, **99**, 053838.

Maddali, S., Calvo-Almazan, I., Almer, J., Kenesei, P., Park, J.-S., Harder, R., Nashed, Y. & Hruszkewycz, S. O. (2018). *Sci. Rep.* **8**, 4959.

Maddali, S., Park, J.-S., Sharma, H., Shastri, S., Kenesei, P., Almer, J., Harder, R., Highland, M. J., Nashed, Y. & Hruszkewycz, S. O. (2020). *Phys. Rev. Appl.* **14**, 024085.

Majid, S. H., Goldan, A. H., Hadji, B., Belev, G., Kasap, S. & Karim, K. S. (2011). *Proc. SPIE*, **7961**, 79614L.

Marshall, M. S. J., Kenesei, P., Marton, Z., Sosa, C., Brecher, C., Wart, M., Miller, S., Singh, B., Miceli, A. & Nagarkar, V. V. (2020). *IEEE Trans. Nucl. Sci.* **67**, 969–973.

Martin, T. & Koch, A. (2006). *J. Synchrotron Rad.* **13**, 180–194.

Marton, Z., Miller, S. R., Brecher, C., Kenesei, P., Moore, M. D., Woods, R., Almer, J. D., Miceli, A. & Nagarkar, V. V. (2015). *Proc. SPIE*, **9594**, 95940E.

Pang, G., Zhao, W. & Rowlands, J. A. (1998). *Med. Phys.* **25**, 1636–1646.

Parsafar, A., Scott, C. S., El-Falou, A., Levine, P. M. & Karim, K. S. (2015). *IEEE Electron Device Lett.* **36**, 481–483.

Pennicard, D., Smoljanin, S., Struth, B., Hirsemann, H., Fauler, A., Fiederle, M., Tolbanov, O., Zarubin, A., Tyazhev, A., Shelkov, G. & Graafsma, H. (2014). *J. Instrum.* **9**, C12026.

Philipp, H. T., Tate, M. W., Shanks, K. S., Purohit, P. & Gruner, S. M. (2020). *J. Instrum.* **15**, P06025.

Que, W. & Rowlands, J. A. (1995). *Med. Phys.* **22**, 365–374.

Samei, E., Flynn, M. J. & Reimann, D. A. (1998). *Med. Phys.* **25**, 102–113.

Scott, C. C. (2019). PhD Thesis, University of Waterloo, Waterloo, Ontario, Canada.

Scott, C. S., Abbaszadeh, S., Ghanbarzadeh, S., Allan, G., Farrier, M., Cunningham, I. A. & Karim, K. S. (2014). *Proc. SPIE*, **9033**, 90331G.

Scott, C. S., Parsafar, A., El-Falou, A., Levine, P. M. & Karim, K. S. (2015). *Proceedings of the IEEE International Electron Devices Meeting (IEDM)*, 7–9 December 2015, Washington, DC, USA. 30.6.1–30.6.4.

Zhao, B. & Zhao, W. (2005). *Med. Phys.* **32**, 128–136.